



Structured ray-wave vector vortex beams in multiple degrees of freedom from a laser

YIJIE SHEN,^{1,2,3,*} XILIN YANG,⁴ DARRYL NAIDOO,^{5,6} XING FU,^{1,2} AND ANDREW FORBES⁶

¹Key Laboratory of Photonic Control Technology (Tsinghua University), Ministry of Education, Beijing 100084, China

²State Key Laboratory of Precision Measurement Technology and Instruments, Department of Precision Instrument, Tsinghua University, Beijing 100084, China

³Optoelectronics Research Centre & Centre for Photonic Metamaterials, University of Southampton, Southampton SO17 1BJ, UK

⁴School of Optics and Photonics, Beijing Institute of Technology, Beijing 100081, China

⁵CSIR National Laser Centre, PO Box 395, Pretoria 0001, South Africa

⁶School of Physics, University of the Witwatersrand, Private Bag 3, Wits 2050, South Africa

*Corresponding author: Y.Shen@soton.ac.uk

Received 18 November 2019; revised 14 May 2020; accepted 20 June 2020 (Doc. ID 382994); published 15 July 2020

Vector vortex beams are conventionally created as the superposition of orbital angular momentum (OAM) modes with orthogonal polarizations, limiting the available degrees of freedom (DoFs) to 2, while their creation by complex optical devices such as metasurfaces, liquid crystals, and interferometers has hindered their versatility. Here we demonstrate a new class of vector vortex beam constructed from four DoFs as multiple ray-like trajectories with wave-like properties, which we create by operating a simple anisotropic microchip laser in a frequency-degenerate state. Our new structure is obtained by the superposition of two stable periodic ray trajectories, simultaneously fulfilling a completed oscillation in the cavity. By a simple external modulation, we can transform our ray trajectories into vortex beams with large OAM, multiple singularities, as well as exotic helical star-shaped patterns. Our experimental results are complemented by a complete theoretical framework for this new class of beam, revealing parallels to hybrid SU(2) coherent states. Our approach offers in principle unlimited DoFs for vectorial structured light with concomitant applications, for example, in engineering classically entangled light and in vectorial optical trapping and tweezing. © 2020 Optical Society of America under the terms of the [OSA Open Access Publishing Agreement](#)

<https://doi.org/10.1364/OPTICA.382994>

1. INTRODUCTION

Vector beams (VBs) with spatially nonseparable polarization have attracted great interest and have recently hatched a myriad of applications. In particular, cylindrical VBs [1] (e.g., radial or azimuthal polarization structures) have been widely applied in optical trapping [2], material processing [3], and communication [4]. A popular method for their creation is to exploit spin-orbit coupling to form the vector vortex beams (VVBs) carrying spin angular momentum (SAM) and orbital angular momentum (OAM), finding many applications [5,6]. Moreover, the space-polarization nonseparable state in VVBs has exotic quantum-like properties [7–12], which has also developed fruitful applications. Using the nonseparable states of VVBs mimicking quantum states, quantum channels can be characterized by classical light [13], which can further realize optical communication with improved capacity and stability [14–16]. The nonseparable state in the interaction between complex VVBs with matter was studied for developing high-speed kinematic sensing and metrology [17–19]. Through generating, characterizing, and measuring more elaborate nonseparable structures in VVBs, *in situ* detection of a cooperative target was recently realized [20]. To date, there were

still rich treasures for exploring more applications in VVBs with this quantum-classical connection.

Therefore, the creation of increasingly structured VBs and VVBs is not only a fundamental scientific endeavor in itself, but is also enabling the way for exciting novel applications. To this end, new structured VBs and VVBs have been designed and tailored, mostly restricted to the higher-order Poincaré sphere [21,22] and hybrid-order Poincaré sphere [23,24], and produced directly from lasers with exotic designs and customized optical elements [25], but more commonly external to the source [6]. These include entanglement-beating VVBs superposed by two general Laguerre–Gaussian (LG) modes with opposite propagation direction to produce an axially varying vector field [26], an SU(2) structured VB as the orthogonally polarized SU(2) coherent states that was generated with an exotic longitudinally varying SAM–OAM coupling [27], and a generalized hyperboloid structured VVB that was proposed to explore the polarization singularities and longitudinal-transverse coupling effects in lasers [28,29]. VVBs with exotic vector vortex lattices were generated, revealing deep fundamental physics of superfluids and Bose–Einstein condensates [30–32]. The photonic wheel structure was proposed to unveil the focused VB with both longitudinal and transverse spin [33,34]. A

novel skyrmion-like structure was recently generated in a focused VVB field, which can be used to realize deep-subwavelength super-resolution imaging [35].

In this paper, we demonstrate a new laser oscillating mechanism together with an external modulation to create a new class of VVB embedded with more degrees of freedom (DoFs). Our laser cavity exploits ray-wave duality to lase on multiple ray-like trajectories, akin to geometric paths inside the cavity, with differing coherent-state phases and independently tunable polarizations. We achieve these states by precise control of the cavity length and off-axis pump position on the anisotropic crystal, the latter to realize polarization control, inside an otherwise empty cavity. By external transformation through simple geometric optics, we demonstrate a new class of structured light with controllable DoFs in trajectory shape, coherent-state phase, OAM, and polarization, producing exotic states of structured light in four DoFs, surpassing the limit of two-dimensional VVBs. We theoretically describe our structured light as the superposition of SU(2) coherent states, revealing a rich parameter landscape for further exploration. Our theoretical and experimental results demonstrate that the prominent hybrid SU(2) geometry of our new beams provide new DoFs for developing new theories and applications of structured beams.

2. HYBRID SU(2) GEOMETRIC ORBITS FROM A LASER

A. Basic Concepts

We will first outline the basic concept behind our work before placing it on a firm theoretical footing in the sections to follow. It is known that when a laser cavity is operated in a frequency-degenerate state, the mode appears to be the result of a ray-like periodic orbit, forming a closed path that is ever repeating [see Fig. 1(a)]. The shape and number of bounces in this trajectory are determined by the cavity length, the cavity mirror curvatures, and the position of the pump light. The output number of “rays” and their directions are likewise determined by the internal trajectories. Although ray-like, they are coherent modes exhibiting a wave-like behavior—we will show that the formalism of SU(2) coherent states is highly appropriate for their description, teasing out the salient properties. Prior to this study, only single geometric modes (trajectories) with a certain transverse size and oscillating phase have been reported, described by just *two* DoFs. Here we present a frequency-degenerate laser capable of generating two geometric modes with different transverse sizes and oscillating phases. Crucially, the two modes oscillate in opposing directions, share the same number of rays, and share a trajectory inflection point at the pump spot as shown in Fig. 1. This allows us to control the polarization state of each by a judicious choice of gain crystal. The result is a new vector state of light described by *four* DoFs and produced directly from a simple laser.

B. Classical Analogy of a SU(2) Coherent State

First, we introduce the property of a quantum coherent state because we will exploit its classical-resembling property that its probability wave packet is coupled with a trajectory of classical movement [36] and expand this property into its classical analogy, i.e., the ray-wave duality of a geometric mode. The coherent state under the SU(2) symmetry group is given by [37]

$$|\phi\rangle = \frac{1}{2^{N/2}} \sum_{K=0}^N \binom{N}{K}^{1/2} e^{iK\phi} |K, N\rangle, \quad (1)$$

where $|K, N\rangle$ represent the set of eigenstates with a constant total boson number of N and ϕ is termed the coherent-state phase. The SU(2) symmetry applied here is the general geometric symmetry of paraxial light beams, which inspires us to propose this for structured light as a classical analogy to the quantum coherent state. To do so, we replace the quantum eigenstates by free-space eigenmodes:

$$|\Psi_{n,m}^{(\phi)}\rangle = \frac{1}{2^{N/2}} \sum_{K=0}^N \binom{N}{K}^{1/2} e^{iK\phi} |\psi_{n+QK,m,l-PK}^{(\alpha,\beta)}\rangle, \quad (2)$$

where the eigenmode $|\psi_{n,m,l}^{(\alpha,\beta)}\rangle$ can be generated by applying SU(2) ladder operators to a fundamental-mode Gaussian beam $|\psi_{0,0,l}\rangle$:

$$|\psi_{n,m,l}^{(\alpha,\beta)}\rangle = \frac{(b_x^\dagger)^n (b_y^\dagger)^m}{\sqrt{n!} \sqrt{m!}} |\psi_{0,0,l}\rangle, \quad (3)$$

$$\begin{bmatrix} b_x^\dagger \\ b_y^\dagger \end{bmatrix} = \begin{bmatrix} e^{-i\alpha/2} \cos(\beta/2) & e^{i\alpha/2} \sin(\beta/2) \\ -e^{-i\alpha/2} \sin(\beta/2) & e^{i\alpha/2} \cos(\beta/2) \end{bmatrix} \begin{bmatrix} a_x^\dagger \\ a_y^\dagger \end{bmatrix}, \quad (4)$$

where $(a_x^\dagger, a_y^\dagger)$ are the linear ladder operators to generate various high-order transverse modes, (α, β) are the two parametric angles in a SU(2) unitary matrix, (n, m) are the transverse-mode indices at the (x, y) plane, and l is the longitudinal-mode index. When $\beta = 0$ or $\beta = \pi$, $|\psi_{n,m,l}^{(\alpha,\beta)}\rangle$ is reduced to a Hermite–Gaussian (HG) mode; when $\alpha = \beta = \pi/2$, it becomes a LG mode [38], and so on. For the superposition to be valid (coherent superposition), the two integers P and Q yield that the eigenmodes $|\psi_{n+QK,m,l-PK}^{(\alpha,\beta)}\rangle$ in Eq. (2) should have a constant eigenfrequency. Akin to the quantum-classical coupling in a coherent state, the classical beams of Eq. (2) have the similar interesting property that the beam wave packet is coupled with the SU(2) geometric ray trajectory, namely, *ray-wave duality*, as a macroscopic manifestation of quantum wave-particle duality.

C. Manipulating SU(2) Geometric Modes

In this section we introduce how to realize these classical SU(2) coherent states as ray-wave geometric beams from a laser. For constructing the well-defined coherent superposition as in Eq. (2), the key issue is the accommodation of a set of eigenmodes with different orders but at the same frequency in a single optical resonator, namely, a *frequency-degenerate state*. This must satisfy the criterion that the ratio of the transverse- and longitudinal-mode frequency spacing is a simple rational number $\Omega = \Delta f_T / \Delta f_L = P/Q$, where P and Q are co-prime integers, and the basic eigenmodes $|\psi_{n+QK,m,l-PK}^{(\alpha,\beta)}\rangle$ construct a frequency-degenerate family (see detailed proof in Section 1 of Supplement 1).

When an optical resonator is close to a frequency-degenerate state, the laser mode and output power would drastically change [39]. Recently, it has been experimentally and theoretically verified that the lasing modes in an off-axis-pumped frequency-degenerate laser cavity have a preference to be localized on periodic ray trajectories. This fulfills the SU(2) re-entrant condition of a two-dimensional coupled oscillator, the trajectories of which for various degenerate states $|\Omega = P/Q\rangle$ are shown in Fig. 1(a).

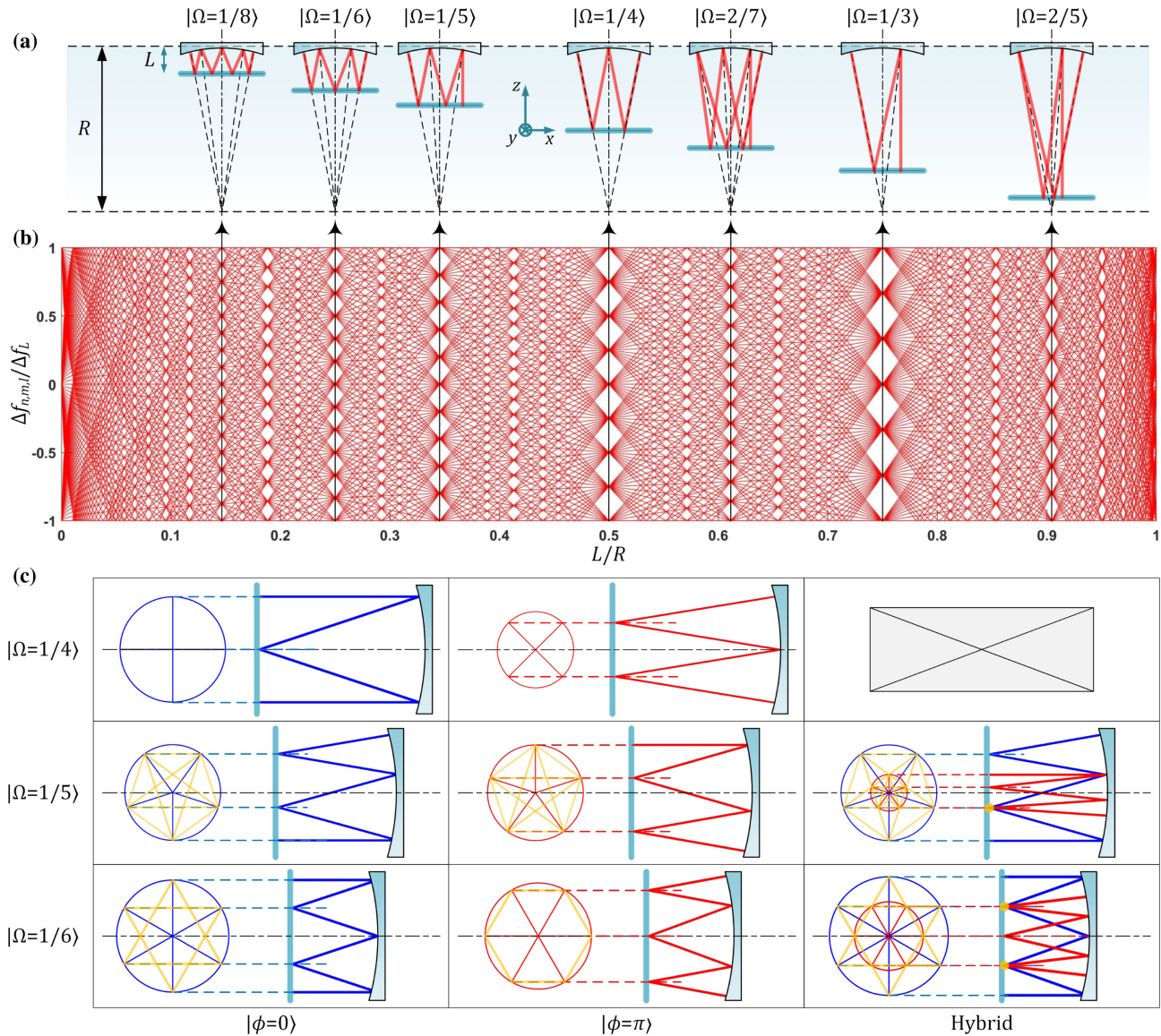


Fig. 1. Frequency degeneracy and SU(2) oscillating orbits. (a) For a concave mirror with a curvature of radius R and a cavity length of L that is precisely controlled, different periodic oscillating trajectories in a cavity with different round-trip periods Q would emerge at some special cavity lengths corresponding to various frequency-degenerate states $|\Omega = P/Q\rangle$. (b) The distribution of frequency-degenerate states can be revealed by the fractal frequency spectrum, i.e., frequency difference ratio $(f_{n,m,l} - f_{n_0,m_0,l_0})/\Delta f_L$ as a function of L/R for the range of $|n - n_0| \leq 12$, $|m - m_0| \leq 12$, and $|l - l_0| \leq 12$, where some degeneracy states $|\Omega = P/Q\rangle$ are marked at corresponding positions. (c) A certain periodic trajectory is determined by not only the degenerate state $|\Omega = P/Q\rangle$ but also the phase state $|\phi\rangle$. For the state $|\Omega = P/Q\rangle$, an auxiliary circle with the vertices of an equilateral Q -gon located on it is helpful to determine the starting points of oscillating orbits, where the starting points at the $z = 0$ plane corresponds to the projection of the vertices on the auxiliary circle. For the two eigenphase states $|\phi = 0\rangle$ and $|\phi = \pi\rangle$, there are always coincident projected vertices. Rotating the auxiliary circle for an angle π/Q of one eigen-phase-state will produce another eigen-phase-state. If the two trajectories of the eigen-phase-states are superposed together and sharing at least a pair of coincident projected points, the hybrid SU(2) oscillating orbits can be obtained, where the yellow auxiliary lines connecting the Q -gon vertices on the auxiliary circle contribute possible coincident projections and result in some equilateral star shape. The yellow dots marked in the hybrid trajectories show the shared coincident projections corresponding to the actual positions of a pump spot in the experimental generation.

Based on this ray-wave duality, the ray-represented modes can also be represented by the corresponding wave packet of the SU(2) quantum coherent state, named SU(2) geometric modes [40–42]. Without loss of generality, hereinafter we consider a plano-concave cavity with a length of L , a concave spherical mirror with radius of curvature R (as the output coupler), and a flat mirror of high reflectivity for the rear mirror. We set the paraxial propagation direction as that of the z axis and the flat mirror as the (x, y) plane with the original point located at the center to form the

Cartesian coordinate system. Ignoring the tiny difference between the physical length and the geometric length, the longitudinal- and transverse-mode spacings are given by $\Delta f_L = c/(2L)$ and $\Delta f_T = \Delta f_L [\tan^{-1}(L/z_R)]/\pi$, respectively, where the Rayleigh range $z_R = \sqrt{L(R-L)}$. The eigenmode frequency of the resonator is the sum of the longitudinal- and transverse-mode frequencies, i.e., $f_{n,m,l} = [l + (n + m + 1)\Omega]\Delta f_L$, where n , m , and l are the orders of the transverse and longitudinal modes.

The frequency degeneracy requires that the allowable eigenmodes should have a constant frequency f_{n_0, m_0, l_0} , and the SU(2) coherent state just fulfills this condition. The distribution of various degenerate states can also be revealed by topological joints in the fractal spectrum [43], i.e., the frequency difference in the neighborhood of the center indices as shown in Fig. 1(b), where some special degenerate states $|\Omega = P/Q\rangle$ are marked and coupled with the periodic orbits in the corresponding degenerate cavities in Fig. 1(a). In general, the ray trajectory should have a round-trip period of Q for the $|\Omega = P/Q\rangle$ state. However, the depicted trajectory is just one instance of an infinite number of possible cases. The shape of a certain trajectory is related not only to the frequency degeneracy but also to the phase of the SU(2) coherent state [44]. Figure 1(c) shows the different trajectories at the two phase states $|\phi = 0\rangle$ and $|\phi = \pi\rangle$ with opposite topological oscillations. For instance, for the $|\Omega = 1/4\rangle$ state, the trajectory is M-shaped when $|\phi = 0\rangle$ and W-shaped when $|\phi = \pi\rangle$; for the $|\Omega = 1/5\rangle$ state, the trajectory is WI-shaped when $|\phi = 0\rangle$ and IW-shaped when $|\phi = \pi\rangle$, and so on.

Note that the phase state $|\Omega\rangle|\phi\rangle$ only specifies the topological shape of the oscillation but not the actual size of it. The actual geometric modes can also have uncertain scales at a certain degeneracy with phase state $|\Omega\rangle|\phi\rangle$, which should be determined by another DoF, i.e., transverse order N [45]. For conveniently describing more detailed geometric modes, we propose the concept of an auxiliary circle for determining the start points of the SU(2) oscillating orbits in a degenerate cavity. The radius of the auxiliary circle \sqrt{N} determines the scale of the geometric mode, which is also related to the actual off-axis displacement of the pump light (see Section 1 of Supplement 1). For the planar geometric mode in the degenerate state $|\Omega = P/Q\rangle$, there are Q auxiliary points on the auxiliary circle with azimuthal angle $\theta_s = 2\pi s/Q + \phi_x$ ($s = 0, 1, 2, \dots, Q-1$) forming an equilateral Q -gon (polygon with Q sides), while the projected points on the $z = 0$ plane are just the start points for the Q th periodic orbits as shown in Fig. 1(c). The auxiliary phase ϕ_x is related to the coherent-state phase by $\phi_x = \phi/Q$. The evolution of this state from $\phi = 0$ to 2π corresponds to the rotation of the auxiliary Q -gon from an angle of 0 to 2π , returning to the initial state. The phase is actually related to the Gouy phase, which can be modulated by astigmatic mode converter systems in experiments [46]. Distinguished from other phase states, the two eigenphase states $|\phi = 0\rangle$ and $|\phi = \pi\rangle$ have the same trajectory for the positive and negative oscillations; also, there are always coincident projections of auxiliary points. For instance, in $|\Omega = 1/5\rangle|\phi = 0\rangle$, there are two kinds of coincident projection, i.e., $s = 1$ with $s = 4$ and $s = 2$ with $s = 3$; for $|\Omega = 1/5\rangle|\phi = \pi\rangle$, $s = 0$ with $s = 4$ and $s = 1$ with $s = 3$; for $|\Omega = 1/6\rangle|\phi = 0\rangle$, $s = 1$ with $s = 5$ and $s = 2$ with $s = 4$; for $|\Omega = 1/6\rangle|\phi = \pi\rangle$, there are three kinds of coincident projection, i.e., $s = 0$ with $s = 5$, $s = 1$ with $s = 4$, and $s = 2$ with $s = 3$ [see the dashed lines marked for various projection pairs in Fig. 1(c)].

We mark all such point pairs by connected lines in Fig. 1(c), which can form exotic star-shaped patterns. Beyond aesthetics, the coincident projected points have a clear physical significance, namely, the inflection point of the bouncing orbit at the flat mirror in the cavity. In an off-axis pumped degenerate cavity, a coincident projected point is usually located at the pump spot rather than the isolated projected point due to the mode matching [44,47]. Therefore, we can adjust the location of the coincident projected point of a geometric mode by off-axis pumping so as to control the

transverse scale parameter N . In other words, this mathematical and geometric representation has practical relevance: from it we understand where to pump the crystal in order to excite specific combinations of trajectories with associated sizes.

Figure 2(a) illustrates control of an SU(2) oscillation in our experiment with a resonator configured for the $|\Omega = 1/4\rangle$ degenerate state, while the pump spot can be adjusted to some desired coincident projected point to adjust the transverse scale. The gain medium was a thin-slice *c*-cut Nd:YVO₄ crystal with an inner surface antireflective (AR) coating for the laser light and an outer surface AR coated for the pump light and high-reflective coated for the laser light. This allows anisotropic refractive indices and stimulated emission cross sections in (x, z) plane [48]. Therefore, the geometric orbit oscillations in our cavity undergo trajectory-dependent polarization modulation in addition to transverse adjustment. To realize vector geometric beams, we exploit the birefringence dependence on the incident angle, shown in Fig. 2(b). Finally, using an astigmatic mode converter constituted by the two cylindrical lenses shown in Fig. 2(c), a planar geometric mode can be converted into a vortex geometric mode. For the vortex geometric modes, the SU(2) rotational symmetry can be directly observed in natural space, which is also a macroscopic manifestation of OAM. Thus, the spatial twisted trajectories can be directly measured via scanning by a charge-coupled device (CCD) camera (see Section 7, Methods, for more details), in contrast to the conventional circular vortex beams where the twisted effect cannot be directly observed and requires other techniques, e.g., interferometry.

In summary, a planar geometric mode in a degenerate cavity should be completely determined by a SU(2) coherent state $|\Omega\rangle|N\rangle|\phi\rangle$ with three DoFs: frequency-degeneracy Ω , transverse order N , and phase ϕ . After mode conversion, a planar geometric mode is transformed into vortex mode represented by $|\Omega\rangle|\ell\rangle|\phi\rangle$, where the OAM index ℓ replaces the transverse order of the planar mode.

D. Hybrid SU(2) Geometric Modes

Next, we demonstrate a hybrid-trajectory state by forcing the laser to oscillate on two different trajectories with orthogonal transverse orders and coherent-state phases simultaneously, to form the new nonseparable state

$$|\psi\rangle = |\psi_1\rangle + |\psi_2\rangle = |\Omega\rangle|N_1\rangle|\phi\rangle + |\Omega\rangle|N_2\rangle|\phi + \pi\rangle. \quad (5)$$

The transverse orders of the two component modes N_1 and N_2 yield a mathematic relationship enabling the two decomposed trajectories to share at least a point of coincident projection, that is, $N_i/N_j = \cos^2(2\pi/Q)/\cos^2(\pi/Q)$ with $\{i, j\} = \{1, 2\}$, while the larger N corresponds to the outer trajectory and the smaller the inner. This state is achieved by locating the pump light at the shared coincident projection of the two trajectories. The hybrid SU(2) orbits can only exist when $Q \geq 5$, because you cannot find the shared coincident projection when $Q \leq 4$ (see Section 2 of Supplement 1 for detailed derivations). The diagrams in the third column of Fig. 1(c) illustrate the formation of hybrid SU(2) orbits with the help of the auxiliary circle demonstrating the shared coincident projected point. Similar to the pure SU(2) geometric modes, the hybrid SU(2) geometric modes can also be converted into vortex beams carrying OAM. Figures 2(d) and 2(e) depict the converted vortex trajectories for the degenerate states $|\Omega = 1/5\rangle$

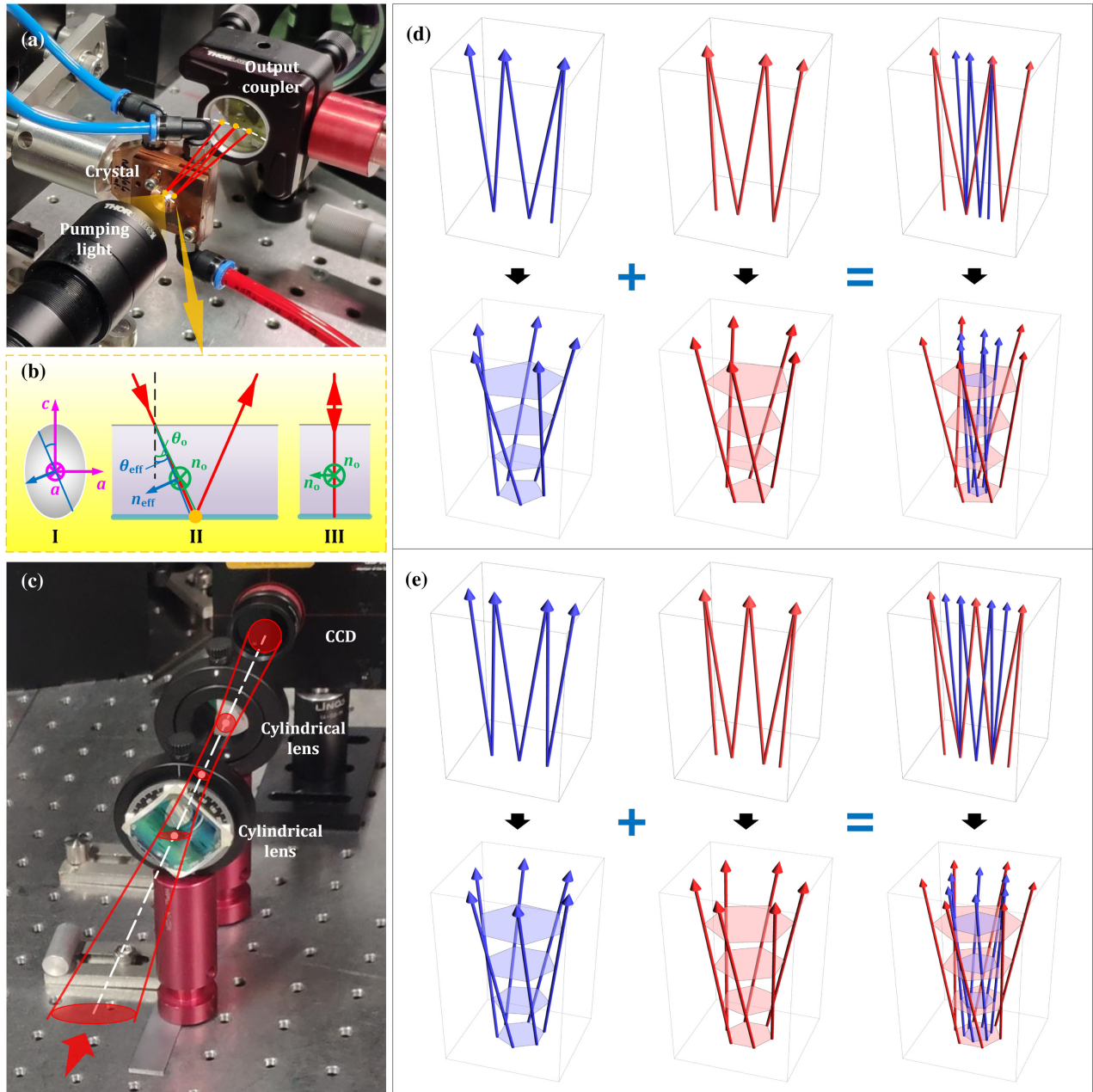


Fig. 2. Controlling planar and vortex SU(2) geometric orbits. (a) The experimental setup of generating a SU(2) geometric mode in a degenerate cavity. This is a case of the $|\Omega = 1/4\rangle$ state, and the period-4 oscillating orbits are schematically depicted in the cavity. (b) A schematic of the birefringent effects for the geometric beams in c-cut Nd:YVO₄. I. The index ellipsoid is depicted for determining the effective refractive index of an input beam. II. For an obliquely incident beam, the vertical and horizontal polarized components yield ordinary and effective refractive indices, respectively, and this difference can introduce a polarization modulation effect in the light beam. III. For normal incidence, there would not be a polarization modulation because there is always an ordinary refractive index. (c) The planar geometric modes can be converted into corresponding vortex geometric modes via focusing it into an astigmatic mode converter constituted by two cylindrical lenses. The illustrations of the formation of hybrid SU(2) trajectories for both cases of planar and vortex geometric modes are theoretically depicted at degenerate states (d) $|\Omega = 1/5\rangle$ and (e) $|\Omega = 1/6\rangle$, where the plot range of the z axis is from 0 to L .

and $|\Omega = 1/6\rangle$, where the first two columns show the pure SU(2) trajectories for the two eigenphase states, and the third column shows the hybrid trajectories. According to SU(2) rotational symmetry, the evolution of phase state $|\phi\rangle$ for vortex geometric modes just corresponds to the axial rotation with an angle of ϕ/Q . Yielded by the coincident projection principle, the inner and outer orbits at a propagation plane of a hybrid trajectory just form the equilateral star shape corresponding to the star-shaped auxiliary lines shown in Fig. 1(c).

Figure 3(a) shows the experimental observation of planar hybrid SU(2) geometric modes with corresponding theoretical simulations. In the experiment, we used a series of Fourier lenses to focus the geometric beams with a beam waist outside the cavity. The lenses were adjusted with a controlled Gouy phase of 0 or π so as to keep the decomposed trajectory at eigenphase state $|\phi = 0\rangle$ or $|\phi = \pi\rangle$. Then we moved the CCD camera along the z axis to record the transverse patterns at various propagation distances. Figures 3(b) and 3(c) show the evolution of hybrid SU(2)

vortex geometric modes at $|\Omega = 1/5\rangle$ and $|\Omega = 1/6\rangle$, respectively. There were two kinds of evolutions of hybrid SU(2) trajectories in our experiment. The first case was observed in the $|\Omega = 1/5\rangle$ state, where the outer trajectory was superposed in the process of

enlarging the inner trajectory by increasing the pump's off-axis displacement. The second case was in the $|\Omega = 1/6\rangle$ state, where the trajectory with phase state $|\phi\rangle$ can be switched into another eigenphase state $|\phi + \pi\rangle$ from the process of increasing the pump's

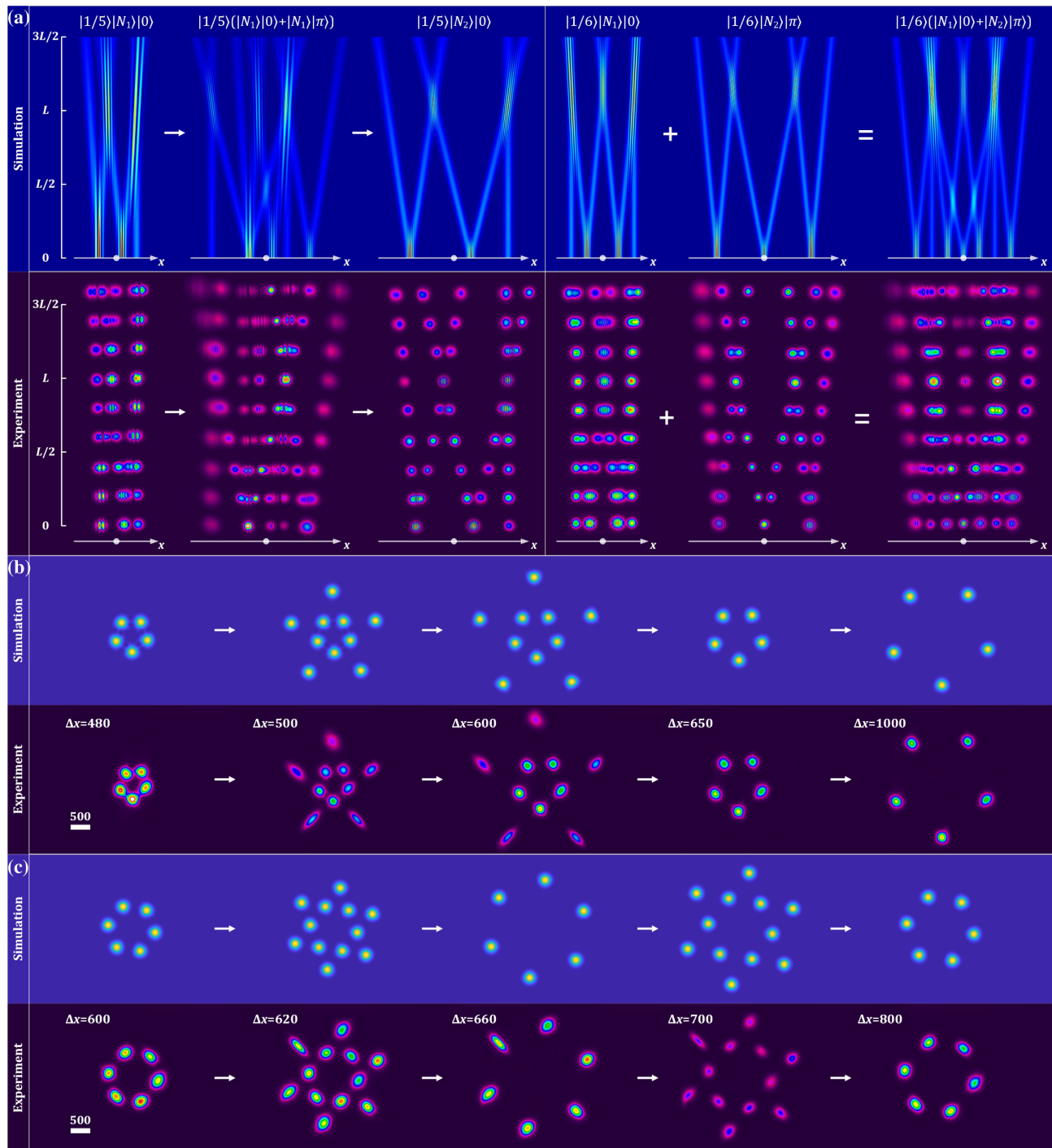


Fig. 3. Generation of hybrid SU(2) geometric modes. (a) The simulated and experimental results of the evolution from a pure SU(2) geometric mode to a hybrid SU(2) geometric mode are shown for the $|\Omega = 1/5\rangle$ and $|\Omega = 1/6\rangle$ states. For the $|\Omega = 1/5\rangle$ state, the hybrid SU(2) orbits appear at the transition from smaller-scale to larger-scale $|\phi = 0\rangle$ orbits, where the $|\phi = 0\rangle$ orbit is continuously varying and a larger-scale $|\phi = \pi\rangle$ orbit is added, forming the hybrid orbit. For the $|\Omega = 1/6\rangle$ state, the hybrid SU(2) orbits appear at the transition from the smaller-scale $|\phi = 0\rangle$ to the larger-scale $|\phi = \pi\rangle$ orbits, where the $|\phi = 0\rangle$ orbit is switched into another $|\phi = \pi\rangle$ orbit and they exist simultaneously at the transition state. (b) The simulated and experimental results of the evolution of hybrid SU(2) geometric modes for the $|\Omega = 1/5\rangle$ state (see the experimentally recorded dynamic process in Visualization 1) and (c) that for the $|\Omega = 1/6\rangle$ state (see the experimentally recorded dynamic process in Visualization 2), where the experimental patterns are marked with the corresponding actual pump off-axis displacement Δx , and the experimental results in figures (b) and (c) are captured near the beam waist with the white bars marked at the bottom left showing the scale for reference of the beam size [unit: micrometers (μm)].

off-axis displacement, and the hybrid trajectory can be obtained by the superposition of the two pure trajectories during the switching. The first-case hybrid trajectory appeared at the region of Δx from 490 to 610 μm for the $|\Omega = 1/5\rangle$ state. There are two regions of the second case where the hybrid trajectory appeared around $\Delta x = 620 \mu\text{m}$ and $\Delta x = 700 \mu\text{m}$, respectively. It is proved that the hybrid SU(2) geometric modes can be stably operated in the corresponding hybrid-trajectory regions. The dynamic processes of generating hybrid SU(2) geometric modes were recorded in [Visualization 1](#) and [Visualization 2](#). The theoretical methods for hybrid SU(2) vector geometric modes are demonstrated in Section 3 of [Supplement 1](#). The detailed experimental and theoretical analysis for the polarization and mode evolution for the SU(2) beams are discussed in Section 4 of [Supplement 1](#).

3. HYBRID SU(2) VECTOR VORTEX BEAMS

Finally, we bring all the tools together, using multiple trajectory control and polarization control to demonstrate a new nonseparable state in multiple DoFs:

$$|\psi\rangle = |\psi_1\rangle + |\psi_2\rangle = |\Omega\rangle|N_1\rangle|\phi\rangle|H\rangle + |\Omega\rangle|N_2\rangle|\phi + \pi\rangle|V\rangle, \quad (6)$$

where $|H\rangle$ and $|V\rangle$ are the horizontal and vertical linear polarization states. Again, the transverse order can be transformed into OAM, resulting into the hybrid SU(2) VVB:

$$|\psi\rangle = |\psi_1\rangle + |\psi_2\rangle = |\Omega\rangle|\ell_1\rangle|\phi\rangle|H\rangle + |\Omega\rangle|\ell_2\rangle|\phi + \pi\rangle|V\rangle, \quad (7)$$

and thus we open up new DoFs for our VVB in contrast to the conventional VVB of $|\ell_1\rangle|H\rangle + |\ell_2\rangle|V\rangle$ mapped on a 2D Poincaré sphere [21,23].

For $|\Omega = 1/5\rangle$, when $\Delta x \leq 480 \mu\text{m}$, the bouncing orbits in the cavity have very small inclined angles such that the birefringent modulation is weak; consequently, the horizontal and vertical polarizations are nearly equal, and the output mode is circularly polarized. When Δx is slightly greater than 480 μm , the outer trajectory is horizontally polarized, while the inner is circularly polarized. This is comprehensible as the two trajectories have different transverse sizes coupled with different birefringent effects in the anisotropic cavity. When Δx is further increased to 610 μm , the outer trajectory can gradually change into a vertically polarized state. When Δx is slightly larger than 610 μm , the outer trajectory vanishes with a pure inner trajectory left. The polarization switching phenomenon can still occur for the pure geometric mode without a hybrid trajectory if Δx is further increased.

Similarly, for $|\Omega = 1/6\rangle$, when $\Delta x \leq 480 \mu\text{m}$, the bouncing orbits have very small inclined angles, and the components of the horizontal and vertical polarizations are nearly equal. While Δx is further increased until 610 μm , the geometric mode is gradually transformed into vertical linear polarization. When Δx is around 620 μm , the hybrid SU(2) trajectory is generated, where the original inner trajectory gradually vanishes and the outer trajectory emerges with the same vertical linear polarization. During $640 \mu\text{m} \leq \Delta x \leq 680 \mu\text{m}$, the output mode is a vertically polarized pure SU(2) geometric mode with a switched phase state rather than the original state. When Δx is around 700 μm , the hybrid SU(2) trajectory is generated again, where the original outer trajectory gradually vanishes and the inner trajectory emerges with a horizontal linear polarization, which is orthogonal to the polarization of the immediately vanished inner trajectory. The

polarization switching phenomenon can still occur in the process of further enlarging of the pure geometric trajectory if Δx is further increased.

Naturally, we can obtain some exotic VVBs and corresponding VVBs with a mode converter in the above process. Same as the pure SU(2) vortex beams, where the OAM effect can be directly observed by their twisted structure with SU(2) rotational symmetry along the propagation axis, the hybrid SU(2) vortex beams also have the twisted structure in their spatial wave packets as shown in Figs. 4(a) and 4(b). Figures 4(c) and 4(d) show our experimental and theoretical results of four typical hybrid SU(2) vortex beams generated at the $|\Omega = 1/5\rangle$ state with $\Delta x = 600 \mu\text{m}$ and $\Delta x = 500 \mu\text{m}$ and at the $|\Omega = 1/6\rangle$ state with $\Delta x = 700 \mu\text{m}$ and $\Delta x = 620 \mu\text{m}$, which are named beams A, B, C, and D, respectively, for convenient description. The results show that these four hybrid SU(2) vortex beams have different vectorial properties with respect to each other. Beams A, B, and C are three kinds of hybrid SU(2) VVBs, and beam D is a hybrid SU(2) scalar vortex beam. For beam A [Fig. 4(c)], the inner orbits are circularly polarized, and thus their beam intensities are independent of the orientation of the polarizer; the outer orbits are vertically linearly polarized, and thus their beam intensities vanish for the horizontal orientation of the polarizer with a maximum for the vertical orientation. For beam B [Fig. 4(d)], the inner orbits are still circularly polarized, while the outer orbits are horizontally linearly polarized. In degenerate state $|\Omega = 1/6\rangle$, we can observe the interesting vector structure where the inner and outer trajectories have orthogonal polarizations as illustrated in beam C. For beam C [Fig. 4(e)], the inner orbits are horizontally polarized and the outer orbits vertically polarized. Thus, the VB C would be reduced into a horizontally polarized scalar SU(2) mode through a horizontally orientated polarizer and another vertically polarized scalar SU(2) mode with opposite phase state through a vertically orientated polarizer. Besides the hybrid SU(2) VB, the hybrid SU(2) scalar beam can also be obtained as beam D [Fig. 4(f)], which is a stable vertically polarized scalar vortex beam.

4. POLARIZATION SINGULARITIES AND TOPOLOGICAL PHASE

Hybrid SU(2) VVBs have exotic properties of polarization singularities and topological phase. For describing the topological properties of the vectorial fields in hybrid SU(2) VVBs, we define two kinds of phase parameters: (1) $\Theta_1 = \arctan(|E_x|/|E_y|)$ and (2) $\Theta_2 = \arg(E_x/E_y)$, where E_x and E_y are the horizontal and vertical components of the electric field. Θ_1 reveals the distribution varying different linear and circular polarization, ranging from 0 to $\pi/2$. $\Theta_1 = 0$ and $\pi/2$ represent the horizontal and vertical linear polarizations, respectively, and $\Theta_1 = \pi/4$ the circular polarization. Θ_2 can unravel more vector properties including the orientation and chirality of polarization, ranging from $-\pi$ to π , which can depict the distribution of polarization singularities of the vectorial field. For a scalar beam, Θ_2 is just reduced to the phase distribution of the light field. Figures 5(a)–5(d) show the distributions of Θ_1 for beams A–D. For each hybrid SU(2) VVB A–C [Figs. 5(a)–5(c)], the different polarizations at the inner and outer trajectory regions are clearly demonstrated with the critical region of chaotic polarized states along a star-shaped line. For the scalar beams like beam D [Fig. 5(d)], Θ_1 is a constant. Θ_1 can only reveal the basic shape of polarization because it is expressed by the magnitude of

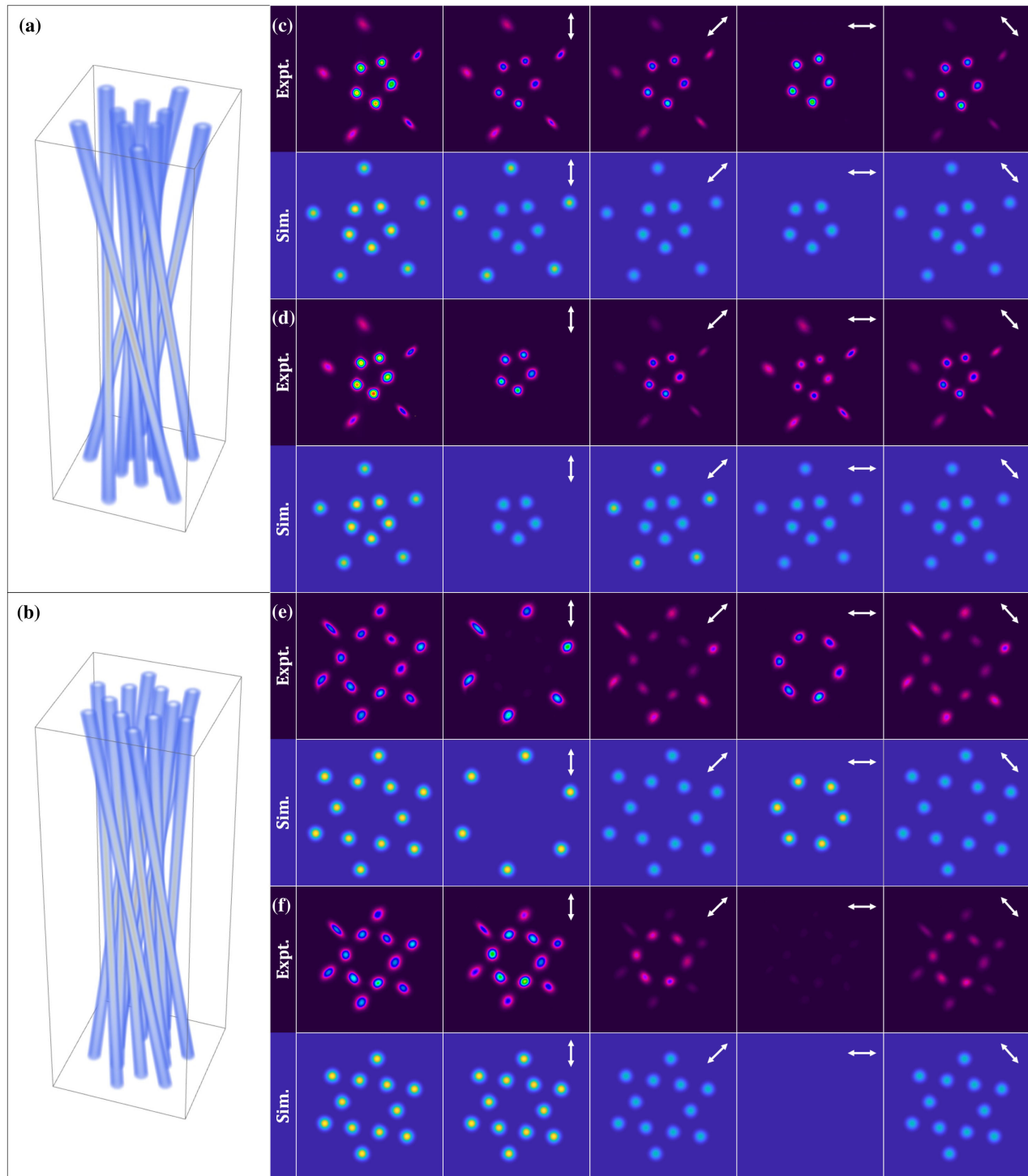


Fig. 4. Vectorial properties of hybrid SU(2) vortex beams. (a),(b) The theoretical 3D wave packet of hybrid SU(2) vortex beams is plotted with clear hyperbolic twisted structures for the (a) $|\Omega = 1/5$ and (b) $|\Omega = 1/6$ states, where the plot range of the z axis is from $-2L$ to $2L$. (c)–(f) The experimental and theoretical results of the transverse patterns (first column) with a measure after a polarizer at four different orientations (2nd to 5th columns) for the beams generated at (c) the $|\Omega = 1/5$ state with $\Delta x = 600 \mu\text{m}$ and (d) $\Delta x = 500 \mu\text{m}$, and at the (e) $|\Omega = 1/6$ state with $\Delta x = 700 \mu\text{m}$ and (f) $\Delta x = 620 \mu\text{m}$, where the white arrows indicate the linear polarizer orientations (vertical, diagonal, horizontal, and antidiagonal directions).

the electric field. An actual polarization state should be completely described by the shape, orientation, and chirality; thus, Θ_2 related by the full complex amplitudes of the electric components can manifest a more refined topological structure in a vectorial field. Figures 5(e)–5(h) show the distributions of Θ_2 for beams A–D.

For beams A and B [Figs. 5(e) and 5(f)], almost all the polarization singularities are distributed in the outer trajectory regions, while the singularities at the corresponding region essentially have opposite topological charges because the outer trajectories just have orthogonal polarization for the two hybrid SU(2) VVBs. For beam C [Fig. 5(g)], whose inner and outer trajectories have

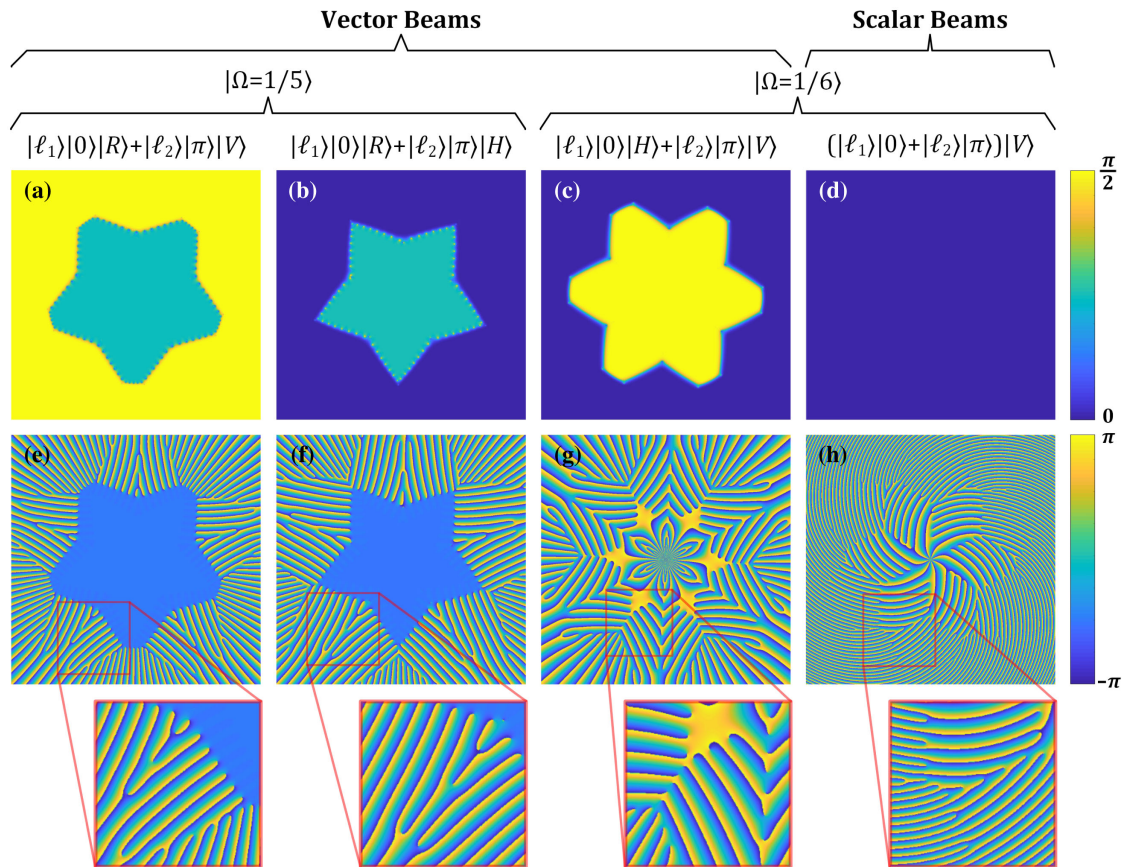


Fig. 5. Polarization singularities and topological phase of hybrid SU(2) vortex beams. (a)–(d) The distributions of phase difference angle defined by $\Theta_1 = \arctan(|E_x|/|E_y|)$ for beams A–D, which show that the beams A–C are VBs and beam D is a scalar beam. (e)–(h) The distributions of phase difference angle defined by $\Theta_2 = \arg(E_x/E_y)$ for beams A–D, which demonstrate the distribution of polarization singularities (for VBs A–C) and phase singularities (for scalar beam D), where the insets show zoomed-in details.

orthogonal polarizations, the polarization singularities are fruitfully distributed over the entire field with a beautiful flower shape. For each of the three beams A–C, the topological phase is induced by a spin-to-orbital coupled effect because it is a superposition of the two trajectories with different SAM and OAM. In the scalar beam D [Fig. 5(h)], the SAM or polarization is separable, and Θ_2 is just the phase distribution of scalar light with multiple phase singularities, where a large OAM is manifested. The clarification of polarization singularities and topological phase is very helpful for extending these new hybrid SU(2) structured beams in applications such as optical tweezers and assembly and exploration of novel manipulating technologies.

5. DISCUSSION

If higher-order hybrid SU(2) trajectories with more oscillating periods ($Q \geq 7$) could be generated, more intriguing properties would be unveiled. As demonstrated above, a hybrid SU(2) trajectory cannot be composed when $Q \leq 4$, and there is only one morphology of a hybrid SU(2) superposed trajectory when $Q = 5, 6$. However, for higher-order degenerate states with $Q \geq 7$, there would be multiple possible cases of hybrid SU(2) trajectories because more inflection points (in the decomposed trajectory) provide more combinations of sharing a pumping spot. Theoretically, there would be two kinds of hybrid SU(2) trajectories for the degenerate states of $|\Omega = 1/7\rangle$ and $|\Omega = 1/8\rangle$, and four kinds of

hybrid trajectories for $|\Omega = 1/9\rangle$ and $|\Omega = 1/10\rangle$, as shown in Figs. 6(a)–6(d), respectively. We presented the theory for obtaining the trajectory-combination number for an arbitrary degenerate state shown in Section 2 of Supplement 1. Moreover, besides the two-trajectory superposition, the hybrid superposition with multiple SU(2) trajectories is also possible to form even higher-order degenerate states, e.g., the three-trajectory-superposed hybrid SU(2) mode shown in Fig. 6(e). Due to the limit of the crystal size in our experiment, it is difficult to control higher-order hybrid SU(2) trajectories when $Q \geq 7$. Therefore, there is still a multitude of exotic properties of hybrid SU(2) modes that need to be theoretically and experimentally explored in the future.

The additional DoFs in our hybrid SU(2) VVB allow us to break the two-dimensional limit inherent in conventional VBs, opening up exciting prospects for applied and fundamental studies. For example, while their SU(2) description is complete, we believe it may be possible to use techniques that map structured beams to Poincaré-like spheres [49–51] to gain insight into how to elegantly represent this new family of hybrid SU(2) VVBs geometrically. That may yield insight into other relations and dynamics, since multidimensional structured light has remained largely unexplored. The strong trajectory nature of our light may aid studies in trajectory-spin coupled processes in the spin-Hall effect of light [52], while the nonseparability of our beam with more DoFs opens for the first time the possibility to classically simulate multipartite high-dimensional quantum processes, including

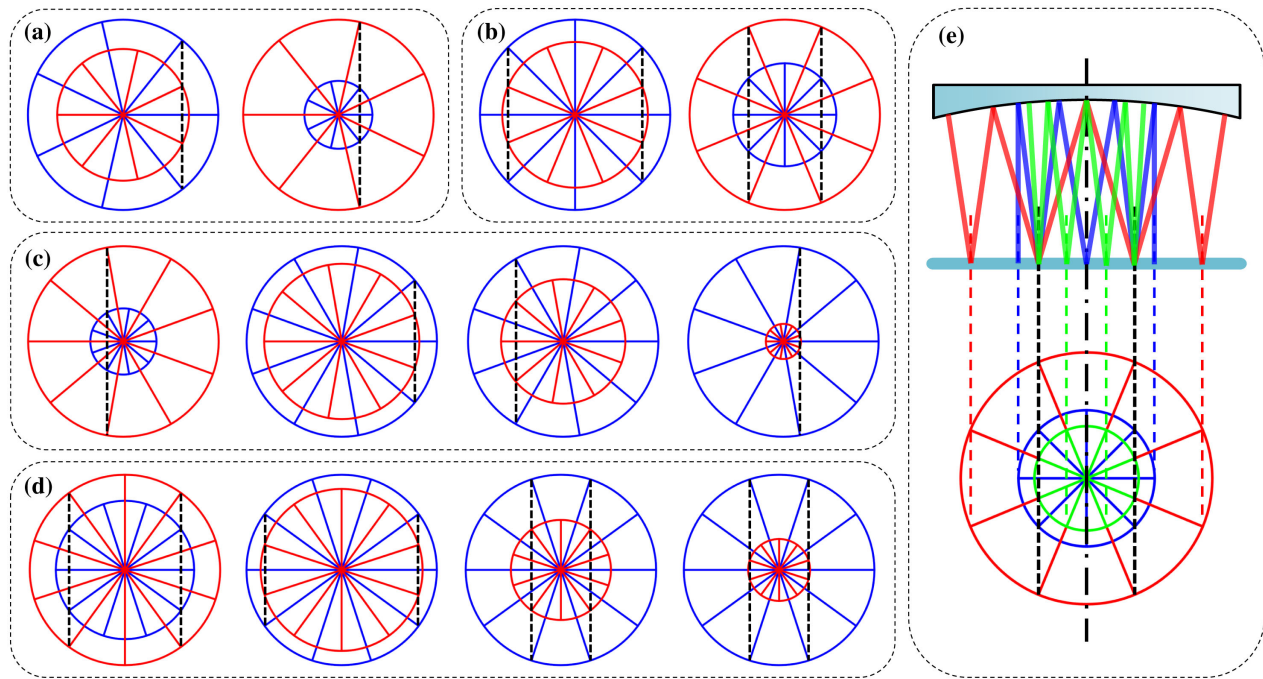


Fig. 6. Complicated hybrid SU(2) modes with multiple trajectory-combination numbers and multitrajectory superposition. (a)–(d) The auxiliary-circle representations of the possible hybrid trajectories for degenerate states (a) $|\Omega = 1/7\rangle$, (b) $|\Omega = 1/8\rangle$, (c) $|\Omega = 1/9\rangle$, and (d) $|\Omega = 1/10\rangle$. (e) The auxiliary circle with intracavity oscillation trajectory representation for a complicated hybrid SU(2) mode superposed by three decomposed SU(2) trajectories at $|\Omega = 1/8\rangle$ state. The black dashed lines represent the coincident inflection points (shared pumping spots) of the three decomposed SU(2) trajectories in a hybrid SU(2) mode.

Greenberger–Horne–Zeilinger (GHZ) states, NOON states, and W states, all of which have been suggested theoretically [8] but not yet demonstrated due to the inability to extend beyond just qubits with vector states of light. Other possibilities include considering the simulation of squeezed state in classical light, a detailed study of polarization singularities and their families in such fields, and propagation dynamics, all of which are logical next steps of study.

6. CONCLUSION

In conclusion, we proposed a new kind of vectorially structured light in four DoFs and showed how to create it directly from a simple laser cavity. Our hybrid SU(2) geometric mode is constituted by two decomposed pure SU(2) mode states with special superposition conditions, fulfilling a complete ray-trajectory oscillation condition, which largely enriches the general families of both intracavity and free-space modes. We also experimentally generated various examples of SU(2) VVBs in various degenerate states ($|\Omega = 1/5\rangle$ and $|\Omega = 1/6\rangle$). The resulting light was tailored to be exotic star-shaped geometric patterns with complex phase and polarization singularities, which is the first demonstration of such structured light beams to our knowledge. Importantly, our hybrid SU(2) VVBs are represented and controlled in multiple DoFs, surpassing the limit of two-dimensional conventional VVBs. Besides conventional DoFs of amplitude, phase, OAM, and polarization, many new DoFs are hatched such as ray-wave orbits, coherent-state phase, and trajectory combination, offering intriguing prospects of unlimited dimensionality controls in such VVBs. Moreover, the simple and elegant at-the-source generation scheme paves ways to extended applications, including simulations of quantum processes with classical light.

7. METHODS

The front end was a laser oscillator where the cavity length can be precisely controlled. Through controlling the off-axis pumping position, various SU(2) geometric modes can be generated. A 808 nm fiber-coupled laser diode (LD) (FOCUSLIGHT, FL-FCSE08-7-808-200) was used as the pump source. With a telescope system with magnification of about 1:1 constituted by two identical AR-coated lenses (focal length $F = 25$ mm), the pump light was focused into a c-cut Nd:YVO₄ slice-like crystal with dopant of 0.5 at.% and thickness of 5 mm, which was wrapped in a copper heat sink and conductively water cooled at 18°C. The outside surface of the crystal was AR coated at 808 nm and high-reflective coated at 1064 nm, and the inner surface was AR coated at 1064 nm. A plano-concave mirror was used as the output coupler, where radius of curvature was 100 mm, and the transmittance was 10% at 1064 nm for the inner surface and AR for the outside surface. In our whole experiment, the pumping power was fixed at about 5.5 W. For measuring the ray trajectories, we used a CCD camera to capture and scan the transverse pattern at different propagation distances along the z axis. In contrast to the conventional circular vortex beams, the OAM of SU(2) structured beams can be directly unveiled by the spatially twisted trajectories captured by the CCD scanning (see more details in Section 5 of Supplement 1). The CCD camera (Spiricon SP620U) is comprised of 1600×1200 pixels with a pixel pitch of $4.4 \mu\text{m}$, corresponding to a charge-coupled screen size of $7.04 \times 5.28 \text{ mm}^2$. In the measurement, the beam diameter size within Rayleigh range was confirmed to be less than 5 mm, so that we could scan the full information of the measured beam propagating within the whole Rayleigh range.

Funding. National Natural Science Foundation of China (61975087); Natural Science Foundation of Beijing Municipality (4172030).

Acknowledgment. Dr. Yijie Shen thanks Prof. Carmelo Rosales-Guzmán at Harbin University of Science and Technology for helpful discussions.

Disclosures. The authors declare no conflicts of interest.

See [Supplement 1](#) for more theoretical and experimental details; see [Visualization 1](#) for the recorded evolution of hybrid SU(2) geometric modes at $|\Omega = 1/5\rangle$ state; see [Visualization 2](#) for the recorded evolution of hybrid SU(2) geometric modes at $|\Omega = 1/6\rangle$ state; see [Visualization 3](#) for the demonstration of eigenphase states formation in the SU(2) trajectory oscillation.

REFERENCES

- Q. Zhan, "Cylindrical vector beams: from mathematical concepts to applications," *Adv. Opt. Photon.* **1**, 1–57 (2009).
- V. Shvedov, A. R. Davoyan, C. Hnatovsky, N. Engheta, and W. Krolikowski, "A long-range polarization-controlled optical tractor beam," *Nat. Photonics* **8**, 846–850 (2014).
- T. Omatsu, K. Miyamoto, K. Toyoda, R. Morita, Y. Arita, and K. Dholakia, "A new twist for materials science: the formation of chiral structures using the angular momentum of light," *Adv. Opt. Mater.* **7**, 1801672 (2019).
- Y. Zhao and J. Wang, "High-base vector beam encoding/decoding for visible-light communications," *Opt. Lett.* **40**, 4843–4846 (2015).
- Y. Shen, X. Wang, Z. Xie, C. Min, X. Fu, Q. Liu, M. Gong, and X. Yuan, "Optical vortices 30 years on: OAM manipulation from topological charge to multiple singularities," *Light Sci. Appl.* **8**, 90 (2019).
- C. Rosales-Guzmán, B. Ndagano, and A. Forbes, "A review of complex vector light fields and their applications," *J. Opt.* **20**, 123001 (2018).
- R. J. C. Spreeuw, "A classical analogy of entanglement," *Found. Phys.* **28**, 361–374 (1998).
- A. Aiello, F. Töppel, C. Marquardt, E. Giacobino, and G. Leuchs, "Quantum-like nonseparable structures in optical beams," *New J. Phys.* **17**, 043024 (2015).
- B. N. Simon, S. Simon, F. Gori, M. Santarsiero, R. Borghi, N. Mukunda, and R. Simon, "Nonquantum entanglement resolves a basic issue in polarization optics," *Phys. Rev. Lett.* **104**, 023901 (2010).
- T. Konrad and A. Forbes, "Quantum mechanics and classical light," *Contemp. Phys.* **60**, 1–22 (2019).
- A. Forbes, A. Aiello, and B. Ndagano, "Classically entangled light," *Prog. Opt.* **64**, 99–153 (2019).
- E. Toninelli, B. Ndagano, A. Vallés, B. Sephton, I. Nape, A. Ambrosio, F. Capasso, M. J. Padgett, and A. Forbes, "Concepts in quantum state tomography and classical implementation with intense light: a tutorial," *Adv. Opt. Photon.* **11**, 67–134 (2019).
- B. Ndagano, B. Perez-Garcia, F. S. Roux, M. McLaren, C. Rosales-Guzman, Y. Zhang, O. Mouane, R. I. Hernandez-Aranda, T. Konrad, and A. Forbes, "Characterizing quantum channels with non-separable states of classical light," *Nat. Phys.* **13**, 397–402 (2017).
- B. Ndagano, I. Nape, M. A. Cox, C. Rosales-Guzman, and A. Forbes, "Creation and detection of vector vortex modes for classical and quantum communication," *J. Lightwave Technol.* **36**, 292–301 (2017).
- A. Sit, F. Bouchard, R. Fickler, J. Gagnon-Bischoff, H. Larocque, K. Heshami, D. Elser, C. Peuntinger, K. Günthner, B. Heim, and C. Marquardt, "High-dimensional intracity quantum cryptography with structured photons," *Optica* **4**, 1006–1010 (2017).
- A. E. Wilner, "Vector-mode multiplexing brings an additional approach for capacity growth in optical fibers," *Light Sci. Appl.* **7**, 18002 (2018).
- S. Berg-Johansen, F. Töppel, B. Stiller, P. Banzer, M. Ornigotti, E. Giacobino, G. Leuchs, A. Aiello, and C. Marquardt, "Classically entangled optical beams for high-speed kinematic sensing," *Optica* **2**, 864–868 (2015).
- V. D'ambrosio, N. Spagnolo, L. Del Re, S. Slussarenko, Y. Li, L. C. Kwek, L. Marrucci, S. P. Walborn, L. Aolita, and F. Sciarrino, "Photonic polarization gears for ultra-sensitive angular measurements," *Nat. Commun.* **4**, 2432 (2013).
- F. Töppel, A. Aiello, C. Marquardt, E. Giacobino, and G. Leuchs, "Classical entanglement in polarization metrology," *New J. Phys.* **16**, 073019 (2014).
- X.-B. Hu, B. Zhao, Z.-H. Zhu, W. Gao, and C. Rosales-Guzmán, "In situ detection of a cooperative target's longitudinal and angular speed using structured light," *Opt. Lett.* **44**, 3070–3073 (2019).
- G. Milione, H. Sztul, D. Nolan, and R. Alfano, "Higher-order Poincaré sphere, Stokes parameters, and the angular momentum of light," *Phys. Rev. Lett.* **107**, 053601 (2011).
- D. Naidoo, F. S. Roux, A. Dudley, I. Litvin, B. Piccirillo, L. Marrucci, and A. Forbes, "Controlled generation of higher-order Poincaré sphere beams from a laser," *Nat. Photonics* **10**, 327–332 (2016).
- X. Yi, Y. Liu, X. Ling, X. Zhou, Y. Ke, H. Luo, S. Wen, and D. Fan, "Hybrid-order Poincaré sphere," *Phys. Rev. A* **91**, 023801 (2015).
- R. C. Devlin, A. Ambrosio, N. A. Rubin, J. B. Mueller, and F. Capasso, "Arbitrary spin-to-orbital angular momentum conversion of light," *Science* **358**, 896–901 (2017).
- A. Forbes, "Structured light from lasers," *Laser Photon. Rev.* **13**, 1900140 (2019).
- E. Otte, C. Rosales-Guzmán, B. Ndagano, C. Denz, and A. Forbes, "Entanglement beating in free space through spin-orbit coupling," *Light Sci. Appl.* **7**, 18009 (2018).
- T.-H. Lu and C. He, "Generating orthogonally circular polarized states embedded in nonplanar geometric beams," *Opt. Express* **23**, 20876–20883 (2015).
- Y. Chen, T.-H. Lu, and K. Huang, "Hyperboloid structures formed by polarization singularities in coherent vector fields with longitudinal-transverse coupling," *Phys. Rev. Lett.* **97**, 233903 (2006).
- T.-H. Lu, Y. Chen, and K. Huang, "Generalized hyperboloid structures of polarization singularities in Laguerre–Gaussian vector fields," *Phys. Rev. A* **76**, 063809 (2007).
- Y. Chen, K. Huang, H. Lai, and Y. Lan, "Observation of vector vortex lattices in polarization states of an isotropic microcavity laser," *Phys. Rev. Lett.* **90**, 053904 (2003).
- Y. Chen, T.-H. Lu, and K. Huang, "Observation of spatially coherent polarization vector fields and visualization of vector singularities," *Phys. Rev. Lett.* **96**, 033901 (2006).
- X.-F. Zhou, J. Zhou, and C. Wu, "Vortex structures of rotating spin-orbit-coupled Bose-Einstein condensates," *Phys. Rev. A* **84**, 063624 (2011).
- A. Aiello, P. Banzer, M. Neugebauer, and G. Leuchs, "From transverse angular momentum to photonic wheels," *Nat. Photonics* **9**, 789–795 (2015).
- K. Y. Bliokh, F. J. Rodríguez-Fortuño, F. Nori, and A. V. Zayats, "Spin-orbit interactions of light," *Nat. Photonics* **9**, 796–808 (2015).
- L. Du, A. Yang, A. V. Zayats, and X. Yuan, "Deep-subwavelength features of photonic skyrmions in a confined electromagnetic field with orbital angular momentum," *Nat. Phys.* **15**, 650–654 (2019).
- A. Perelomov, *Generalized Coherent States and Their Applications* (Springer, 2012).
- V. Bužek and T. Quang, "Generalized coherent state for bosonic realization of SU(2) Lie algebra," *J. Opt. Soc. Am. B* **6**, 2447–2449 (1989).
- Y. Chen, Y. Hsieh, and K. Huang, "Originating an integral formula and using the quantum Fourier transform to decompose the Hermite-Laguerre-Gaussian modes into elliptical orbital modes," *OSA Continuum* **1**, 744–754 (2018).
- Y. Chen, J. Tung, P. Chiang, H. Liang, and K. Huang, "Exploring the effect of fractional degeneracy and the emergence of ray-wave duality in solid-state lasers with off-axis pumping," *Phys. Rev. A* **88**, 013827 (2013).
- N. Barré, M. Romanelli, M. Leubental, and M. Brunel, "Waves and rays in plano-concave laser cavities: I. Geometric modes in the paraxial approximation," *Eur. J. Phys.* **38**, 034010 (2017).
- Y. Shen, X. Fu, and M. Gong, "Truncated triangular diffraction lattices and orbital-angular-momentum detection of vortex SU(2) geometric modes," *Opt. Express* **26**, 25545–25557 (2018).
- Y. Shen, Z. Wan, Y. Meng, X. Fu, and M. Gong, "Polygonal vortex beams," *IEEE Photon. J.* **10**, 1503016 (2018).
- J. Tung, P. Tuan, H. Liang, K. Huang, and Y. Chen, "Fractal frequency spectrum in laser resonators and three-dimensional geometric topology of optical coherent waves," *Phys. Rev. A* **94**, 023811 (2016).

44. Y. Shen, X. Yang, X. Fu, and M. Gong, "Periodic-trajectory-controlled, coherent-state-phase-switched, and wavelength-tunable SU(2) geometric modes in a frequency-degenerate resonator," *Appl. Opt.* **57**, 9543–9549 (2018).
45. Y. Chen, S. Li, Y. Hsieh, J. Tung, H. Liang, and K. Huang, "Laser wavepacket representation to unify eigenmodes and geometric modes in spherical cavities," *Opt. Lett.* **44**, 2649–2652 (2019).
46. Y. Shen, Y. Meng, X. Fu, and M. Gong, "Hybrid topological evolution of multi-singularity vortex beams: generalized nature for helical-Ince-Gaussian and Hermite-Laguerre-Gaussian modes," *J. Opt. Soc. Am. A* **36**, 578–587 (2019).
47. Y. Chen, C. Jiang, Y. Lan, and K. Huang, "Wave representation of geometrical laser beam trajectories in a hemiconfocal cavity," *Phys. Rev. A* **69**, 053807 (2004).
48. T.-H. Lu and L. Lin, "Observation of a superposition of orthogonally polarized geometric beams with a c-cut Nd: YVO₄ crystal," *Appl. Phys. B* **106**, 863–866 (2012).
49. M. A. Alonso and M. R. Dennis, "Ray-optical Poincaré sphere for structured Gaussian beams," *Optica* **4**, 476–486 (2017).
50. M. R. Dennis and M. A. Alonso, "Swings and roundabouts: optical Poincaré spheres for polarization and Gaussian beams," *Philos. Trans. R. Soc. London, Ser. A* **375**, 20150441 (2017).
51. M. R. Dennis and M. A. Alonso, "Gaussian mode families from systems of rays," *J. Phys.* **1**, 025003 (2019).
52. X. Ling, X. Zhou, K. Huang, Y. Liu, C.-W. Qiu, H. Luo, and S. Wen, "Recent advances in the spin Hall effect of light," *Rep. Prog. Phys.* **80**, 066401 (2017).